

# Observation-driven model for calculating water harvesting potential from advective fog in (semi-)arid coastal regions

Felipe Lobos-Roco<sup>1,2</sup>, Jordi Vilà-Guerau de Arellano<sup>3</sup>, and Camilo del Río<sup>4</sup>

<sup>1</sup>Centro UC Desierto de Atacama, Pontificia Universidad Católica de Chile.

<sup>2</sup>Facultad de Agronomía y Sistemas Naturales, Pontificia Universidad Católica de Chile.

<sup>3</sup>Meteorology and Air Quality group, Wageningen University, the Netherlands.

<sup>4</sup>Instituto de Geografía, Pontificia Universidad Católica de Chile.

**Correspondence:** Felipe Lobos-Roco (flobosr@uc.cl; felipe.lobos.roco@gmail.com)

## Abstract.

Motivated by finding complementary water sources in (semi-)arid regions, we develop and assess an observation-driven model to calculate fog harvesting water potential. We aim to integrate this model with routine meteorological data collected under complex meteorological and topographic conditions to characterize the advective fog phenomenon. Based on the mass balance principle, the Advective fog Model for (semi-)Arid Regions Under climate change (AMARU) offers insights into fog water harvesting volumes across the temporal and spatial domains. The model is based on a simple thermodynamic approach to calculate the dependence of the liquid water content ( $r_l$ ) on height. Based on climatological fog collection records, we introduce an empirical efficiency coefficient. When combined with  $r_l$ , this coefficient facilitates the estimation of fog harvesting volumes ( $L m^{-2}$ ). AMARU's outputs are validated against in-situ observations collected over Chile's coastal (semi-)arid regions at various elevations and years (2018-2023). The model's representations of the seasonal cycle of fog harvesting follow observations with errors of  $\sim 10\%$ . The model satisfactorily estimates the maximum  $r_l$  ( $\sim 0.8 g kg^{-1}$ ) available for fog harvesting potential in the vertical column. To assess spatial variability, we combine the model with satellite-retrieved data, enabling the mapping of fog harvesting potential along the Atacama coast. Our approach enables the application of the combined observational-AMARU model to other (semi-)arid regions worldwide that share similar conditions. Through the quantification of fog harvesting, our model contributes to water planning, ecosystem delimitation efforts, and the study of the climatological evolution of cloud water, among others.

## 1 Introduction

Water resources in (semi-)arid regions are of critical value for social, economic, and ecological development. However, in recent decades, climate change has enhanced drought periods, intensifying water stress in areas already facing scarcity. This has resulted in a worldwide dryland expansion (Koppa et al., 2023). For example, Chile's (semi-)arid and mediterranean regions have suffered a fifteen-year drought, experiencing a nearly 40% decrease in precipitation (Garreaud et al., 2021). Likewise, other dry regions such as California, South Africa, Australia, Spain, and Morocco are confronting similar challenges related to water scarcity, including new threats like fire increased risks, degradation of soil ecosystems, and impacts on food security

(Goulden and Bales, 2019; Berbel and Esteban, 2019; Keeley and Syphard, 2021; Kogan and Kogan, 2019). Moreover, future  
25 IPCC's climate scenarios are discouraging, projecting even drier conditions by 2050 (Masson-Delmotte et al., 2021). Under  
this escalating water scarcity scenario, the exploration of new water resources is imperative.

In this context, the collection of freshwater from fog presents itself as a viable alternative to face water scarcity, especially in  
(semi-)arid regions along the subtropical western coasts. Fog harvesting has long represented a significant untapped water po-  
30 tential in the world's dry regions (Klemm et al., 2012). For example, in the coastal Atacama Desert, fog and dew represent the  
sole water source across vast territories with almost null precipitations (Cereceda et al., 2008). However, quantifying this water  
potential represents a scientific challenge, requiring a deep understanding of the physical processes controlling the formation  
and dissipation of the marine stratocumulus (Sc) cloud deck over the ocean (Andersen et al., 2020; del Río et al., 2021b),  
its interaction with coastal topography (Lobos-Roco et al., 2018), and the effectiveness of fog collector designs (Verbrugghe  
35 and Khan, 2023). In addition, the lack of available and direct observations of the fog phenomenon, combined with the com-  
plexity of topography, makes it challenging to pinpoint where fog forms, identify optimal harvesting seasons, and determine  
potential yield. Consequently, advancing our knowledge to quantify harvestable water from fog clouds is imperative to develop  
this promising alternative water source. Estimating where, when, and how much water can be harvested from fog is socially  
relevant. Estimating fog water potential can facilitate the transition from experimental fog harvesting practices to industrial  
40 ones (Lobos-Roco et al., 2024), potentially enhancing the development of overlooked desert territories, and benefiting their  
local communities. Moreover, estimating potential fog water production can help us better understand the unique ecosystems  
sustained by fog (Koch et al., 2019; Muñoz-Schick et al., 2001; Moat et al., 2021), contributing to the assessment of their  
conservation status under a rapidly warming climate.

45 Fog is a meteorological phenomenon defined by a boundary layer cloud in permanent contact with the Earth's surface  
(Roach, 1995; Stull, 2012). The origins of fog are influenced by different atmospheric boundary layer and local topographic  
conditions. However, in most of the (semi-)arid regions along the (sub)tropical western margins of continents, fog formation  
is driven by the ocean-to-land advection of the Sc cloud. The Sc cloud forms over the ocean in a vast deck controlled by a  
strong inversion layer resulted from the interaction between the sea surface temperature and large-scale subsidence (Muñoz  
50 et al., 2011). Here, one of the main physical processes involved in stratocumulus formation is the microphysical properties of  
cloud droplets, which are linked to cloud optical properties that have important climate effects (Wood, 2012). In the South East  
Pacific, cloud droplet sizes of 5 to 15  $\mu\text{m}$  are often found, whose concentration is  $\leq 50 \text{ cm}^{-3}$  increasing to  $200 \text{ cm}^{-3}$  along  
coastal areas of Chile (Painemal and Zuidema, 2011). The droplet size and concentration determines the liquid water content  
(Gultepe et al., 2021), which essentially is the amount of water that can be harvested on land once Sc becomes fog. As well  
55 as, the stability of the marine boundary layer (MBL) determines the formation, maintenance, and dissipation of the Sc cloud.  
Formation and maintenance depend on how well-mixed the MBL is in terms of potential temperature ( $\partial\theta/\partial z < 3.1 \times 10^{-3}$   
 $\text{K m}^{-1}$ ) the MBL is, while the dissipation is influenced by its stratification ( $\partial\theta/\partial z > 3.1 \times 10^{-3} \text{K m}^{-1}$ ) (Lobos-Roco et al.,  
2018). This cloud forms at the upper part of the MBL, exhibiting a clear vertical structure. This structure is characterized by an

averaged cloud base ranging from 300 to 400 m (Lu et al., 2007), determined by the lifting condensation level. From the lifting  
60 condensation level to up, the measured liquid water content progressively rises. Based on observations in the same region, we  
take  $\sim 0.7 \text{ g kg}^{-1}$  at cloud top as the maximum value (Schween et al., 2022). The liquid water content abruptly drops to  $0 \text{ g}$   
 $\text{kg}^{-1}$  just above the cloud top, where the air becomes stratified and extremely dry. The Sc cloud is advected into the continent  
by the typical strong thermal-driven sea breeze of (semi-)arid regions (Lobos-Roco et al., 2021). Upon reaching land, the cloud  
deck is affected by local conditions that, together with the high topography, lift it, forming fog belts (del Río et al., 2021b).  
65 Depending on latitude and topography, these fog belts vary in altitude; for example, in the Atacama region, they are found in  
the coastal mountains between 600 and 1200 m ASL (Cereceda et al., 2008; Garreaud et al., 2008). This narrow belt represents  
the area where fog can potentially be harvested.

The harvesting process is performed by nature through specialized plants that accumulate water in their leaves, spines, and  
70 branches, making it available for the soil and roots (Malik et al., 2014; García et al., 2021; Koch et al., 2019). However, fog can  
also be harvested artificially through passive collectors, which efficiently harvest fog water using meshes (Schemenauer and  
Cereceda, 1994). Numerous studies have reported promising fog harvesting volumes worldwide in arid and semi-arid regions.  
For example, rates between  $6\text{-}8 \text{ L m}^{-2} \text{ d}^{-1}$  have been reported in the hyperarid Atacama Desert in Chile (Cereceda et al.,  
2002; Larrain et al., 2002),  $1\text{-}5 \text{ L m}^{-2} \text{ d}^{-1}$  along the western coast of South Africa (Klemm et al., 2012), and  $7 \text{ L m}^{-2} \text{ d}^{-1}$  in  
75 the Iberian Peninsula, Spain (Estrela et al., 2009).

In recent years, significant progress has been made in understanding the spatial variability of Sc cloud and fog (del Río  
et al., 2021b; Andersen et al., 2020), as well as the vertical structure of the fog cloud (García et al., 2021; Lobos-Roco et al.,  
2018) and the practical applications of fog and dew collection in water-stressed regions (Lobos-Roco et al., 2024; Baguskas  
80 et al., 2021). Despite these advancements, there remains a need to integrate these findings into a unified model that can address  
the questions of where, when, and how much water can be harvested from clouds. In this research, we present the **Advective**  
**fog Model for (semi-)Arid Regions Under climate change (AMARU)**, a phenomenological model designed to estimate fog  
harvesting potential volumes continuously in time and space.

## 2 Model formulation and evaluation

85 The AMARU reproduces the fog that can be potentially harvested using standard fog collectors, estimating the liquid water  
content of the air. A particular aspect of AMARU is to apply the available routine meteorological observations to obtain this  
liquid water content. The model is based on the evolution of time and the height of marine stratocumulus adiabatic liquid water  
content moving towards land characterized by complex topography. Figure 1 shows the physical assumptions and processes  
along with the respective variables and units. The model is derived from the mass conservation equation. The sequence of  
90 physical mechanisms is: (i) during a fog event, a certain amount of liquid water ( $W_l$ ) is retained from the total fog inflow when

passing through a passive collector. We assume that the harvested fog water results from the difference between fog inflow ( $F_{in}$ ) and outflow ( $F_{out}$ ) in  $\text{g kg}^{-1} \text{ m s}^{-1}$ . This equation reads as follows:

$$W_h = F_{in} - F_{out}, \quad (1)$$

(ii) Fog inflow and outflow are described as fluxes of the mixing ratio:

$$95 \quad F_{in} = r_l u_x, \quad (2)$$

$$F_{out} = F_{in}(1 - \eta), \quad (3)$$

where  $r_l$  is the liquid water mixing ratio, defined as the amount of liquid water ( $m_l$  in Fig.1) per unit mass of dry air ( $m_d$ ) that contains it, expressed in grams of water per kilogram of dry air ( $\text{g kg}^{-1}$ ). To calculate the inflow we use  $u_x$ , which represents the perpendicular (mean  $\pm$  std) wind speed ( $\text{m s}^{-1}$ ) relative to the collector. (iii) The term  $\eta$  is a dimensionless ratio representing the collector efficiency. This coefficient is described as:

100

$$\eta = \frac{W_h}{F_{in}}, \quad (4)$$

where  $\eta$  corresponds to the percentage of water harvested out of the total water that can potentially pass through the collector (calculation in Section 2.2). Reordering the terms, we express Equation (1) in net terms as:

$$W_h = r_l u_x \eta. \quad (5)$$

105 The  $W_h$  units are then  $\text{g kg}^{-1} \text{ m s}^{-1}$ . However, for the final output, we convert  $\text{L m}^{-2} \text{ s}^{-1}$  (equivalent to mm) once grams are transformed to liters and dry air density ( $\text{kg m}^{-3}$ ) is included as:

$$W_h = r_l \rho_a u_x \eta. \quad (6)$$

Finally,  $W_h$  is integrated over a period as:

$$\overline{W}_h^{\Delta t} = \int_{t_0}^{t_1} W_h dt \quad (7)$$

110 where  $t_0$  and  $t_1$  correspond to the initial and ending times (in seconds). The model has three main assumptions described as follows: (1)  $F_{in} > F_{out}$ ; (2) since the model aims to reproduce advective fog collection, it is assumed that condensation only occurs in the atmosphere under the condition  $r_l = r_v - r_s$ ; (3) the mixing ratio ( $r_v$ ) being two orders of magnitude higher than  $r_l$ , is nearly conserved.

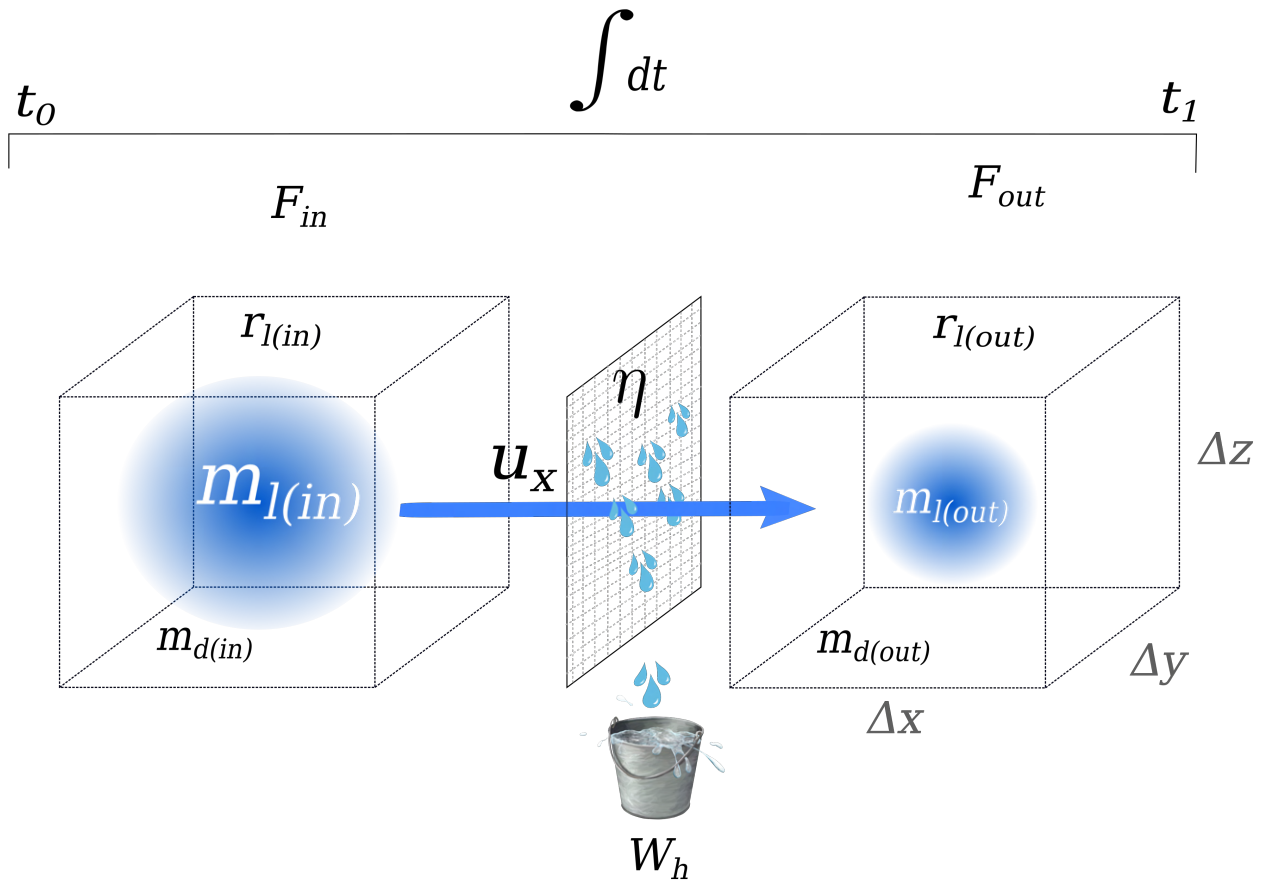


**Figure 1.** AMARU model physical interpretation, including terms from equations (1) to (7).

In Equation (6),  $r_l$  and  $\eta$  depend on location and condensation processes. Regarding location,  $r_l$  varies in height (the vertical dimension of the model) and depends on the conditions of the marine Sc cloud over the ocean and its interaction with the topography. To estimate this variable using routine data, we assume that water vapor condenses once it reaches the thermodynamic conditions to reach saturation, This assumption implies that we do not take microphysical properties such droplet size, nucleation or droplet concentration into the calculations. The second term,  $\eta$  groups cloud microphysics, the collector design, and its material properties. To delve into the detailed calculation of  $r_l$  and  $\eta$ , we break down the analysis of Equation (6) into two parts: the thermodynamic and water potential modules (section 2.1 and 2.2). Additionally, we introduce a third module for representing the model's horizontal spatial variability of  $W_h$  through spatial interpolation creating a fog harvesting potential map.

## 2.1 Thermodynamic module: obtaining liquid water mixing ratio ( $r_l$ )

Liquid water mixing ratio is a complex variable to estimate and measure. It can be obtained from complex and computationally expensive atmospheric models (Large-Eddy Simulation (LES); Weather Research and Forecasting (WRF)) (Bergot, 2016) or by sophisticated and expensive instrumentation (fog measurements devices; microwave radiometers) (Kim et al., 2022; Gulpepe and Milbrandt, 2007). However, our objective here is to estimate  $r_l$  using routine meteorological data. To achieve this, we propose employing the air parcel method (Wetzel, 1990), which calculates thermodynamic changes related to an air parcel as it is uplifted from the surface. The strategy here is to obtain the adiabatic liquid water mixing ratio including the mixing during the lifting. This method has been successfully tested in the Atacama region by Lobos-Roco et al. (2024, 2018), who averaged the meteorological conditions of two meteorological stations located at different heights ( $z_1$  and  $z_2$ ) along a topographic transect. This strategy allows for observation at two-combined points within the MBL during advective fog events:  $z_1$  represents near-surface marine meteorological conditions, while  $z_2$  represents inland meteorological conditions close to the MBL top, where fog formation occurs. Figure 2a schematizes the strategy for estimating  $r_l$  using the parcel method. This estimation involves four steps, which are described and evaluated in the following subsections.

### 2.1.1 Fog frequency

AMARU is a phenomenological model that relies on the presence of advective fog, which typically occurs under a well-mixed MBL regime (Lobos-Roco et al., 2018). We define fog frequency as the number of counts when fog is present over a timestep (in an hour), expressed in percentages. For example, 50%'s fog frequency means that fog occurred during 30 min over an hour. Thus, we propose three criteria for estimating fog frequency using routine meteorological data. The first criterion posits fog frequency when air temperatures reach the dew temperature ( $T_a - T_d = 0$ ). However, this condition has been rarely observed, particularly in the coastal Atacama, even during fog formation. For this reason, we propose and test four alternative thresholds. For this estimation, we exclusively use data from station  $z_2$ . The second criterion is that MBL must be well-mixed. Our criterion for fulfilling this assumption is that the potential temperature gradient ( $\partial\theta/\partial z$ ) between  $\theta_{(z_1)}$  and  $\theta_{(z_2)}$  is minimal. Here, we propose and test four thresholds close to  $0 \text{ K m}^{-1}$ . The third criterion is similar to the second one but employs the specific

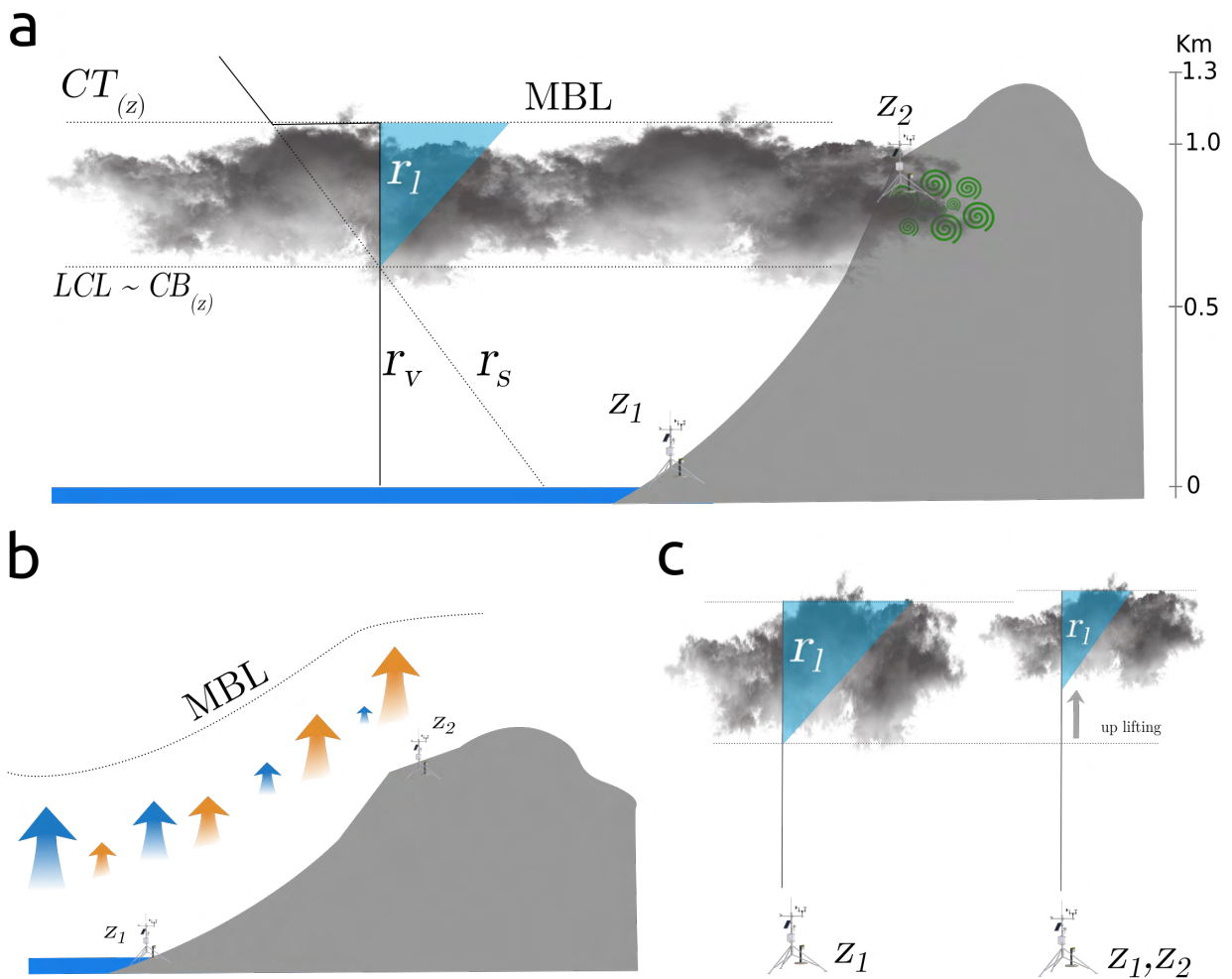


**Figure 2.** (a) Schematic vertical cross-section representing the estimation of liquid water content ( $r_l$ ) using the air parcel method. (b) Physical representation of the topographic uplifting of Sc cloud and its interaction in the ocean-land transition. Blue (orange) arrows indicate latent heat flux (sensible heat flux) from the surface (c). Representation of the combined meteorological conditions from stations  $z_1$  and  $z_2$  at the cloud base, cloud top, and  $r_l$  representation.

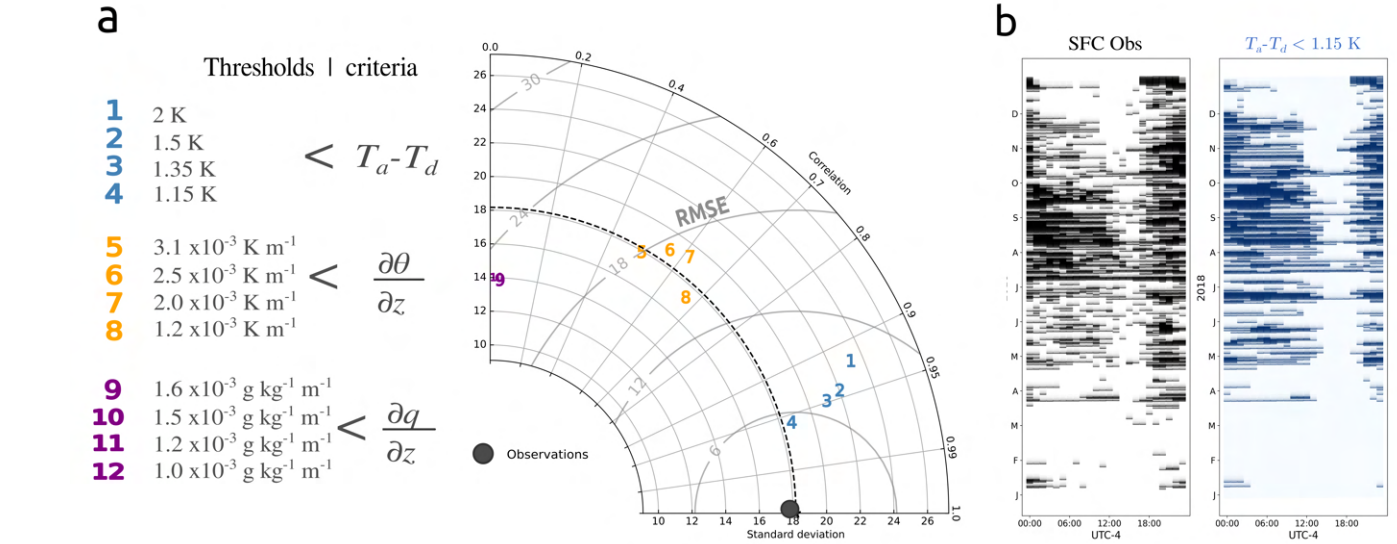


**Figure 3.** (a) Taylor diagram comparing the proposed criteria and thresholds for estimating fog frequency (%). The diagram displays correlation ( $r$ ), standard deviation (in FF units, %), and root mean square error (RMSE in FF units, %) between the criteria-thresholds and observations. The number of data points used is 8760, which corresponds to hourly data over a year. (b) Comparison of the annual diurnal cycle of fog frequency between observations (SFC) in blue and the best-performing criteria in black. Every black/blue mark represents the presence (100% of frequency) at every hour during 2018. Note that numbers 11 and 12 have a slightly negative correlation, placed behind (left) to the Taylor diagram y-axis.

humidity (assumed as mixing ratio) vertical gradient ( $\partial q/\partial z$ ) to assess MBL mixing. Similar to the first criterion we propose and test four thresholds to determine how well-mixed the MBL is in terms of potential temperature and specific humidity.

Figure 3 shows a statistical comparison between the estimated MBL fog frequency (in %) derived from the three proposed criteria and thresholds, and observations obtained from a Standard Fog Collector, SFC (Schemenauer and Cereceda, 1994). The observations are conducted in the fog oases of Alto Patache ( $z_2$ ) within the Atacama Desert during the year 2018 (20.82° S; 70.14° W; 850 m ASL, 5 km from the coast). In addition, we also use data from the meteorological station at Diego Aracena Airport,  $z_1$  (20.52° S; 70.15° W; 48 m ASL), to calculate the vertical gradients.

In general terms, among the three proposed criteria, those based on  $T_a - T_d$  (blues) show the strongest correlation with directly observed fog collection. Among these, the threshold  $T_a - T_d < 1.15 \text{ K}$  (n.4 in Fig. 3a) emerges as the most accurate, exhibiting a standard deviation aligned with observations (18%), a correlation coefficient ( $r$ ) of 0.95, and a root mean square error (RMSE) of 6%. However, the remaining thresholds yield similar results, suggesting that fog occurs when  $T_a - T_d$  spans from 2 to 1.15 K. The second and third criteria are based on the parcel method and the mixing layer theory, which states that Sc cloud formation occurs under well-mixed MBL conditions. The chosen thresholds have been studied before in the coastal Atacama region by Lobos-Roco et al. (2018, 2024), del Río et al. (2021a) and García et al. (2021). The second criterion (depicted in orange) shows promising results when compared to observations, displaying a standard deviation ranging between 17 and 20%,



an  $r$  value ranging from 0.5 to 0.7, and a RMSE of  $\sim 17\%$ . These values suggest that the MBL tends to be thermally well-mixed (exhibiting minimal vertical gradients) during fog presence. The last criterion (purple ones) demonstrates insufficient performance in detecting fog frequency, exhibiting no correlation with observations. The disparity in the correlation between thermal and moisture vertical gradients with fog frequency can be attributed to the aridity of the observation location. On one hand, the arid terrain thermally contributes less to the MBL during fog events (low radiation during the day over the coastal arid zones), showing well-mixed MBL. Conversely, when fog is absent, for example during night, the arid slopes contributes to a stable stratified MBL. On the other hand, the arid landscape does not contribute moisture to the MBL during fog frequency, nor does it when fog is absent, thereby showing no correlation with fog frequency. Figure 3b illustrates the diurnal cycle of fog frequency observed at the Alto Patache fog oasis throughout 2018, as measured by the Standard Fog Collector (SFC) and estimated using the threshold with the best performance (number 4). This threshold successfully estimates fog frequency using simple meteorological data for any day and time throughout the year.

### 2.1.2 Cloud Base, CB

Once fog frequency is estimated, we proceed to calculate the height of the fog-cloud base (CB). This process is summarized in Figure 2. The calculation assumes that the lifting condensation level (LCL) in boundary layer clouds such as Sc is equivalent to the cloud base. To compute this, we adopt two approaches inspired by the parcel method of (Wetzel, 1990). The first approach solely considers data from the lowest station ( $z_1$ ), representative of surface-marine conditions, where LCL corresponds to the height at which the mixing ratio equals to saturated mixing ratio:  $r_v - r_s = 0$ , (Fig. 2a). This LCL represents the CB over the ocean.

The second approach considers two physical processes involved in the Sc-to-fog transition: environmental mixing and topographic uplifting. Firstly, to represent the mixing with the environment experienced by an air parcel during adiabatic ascent, and based on (Lobos-Roco et al., 2018), we combine the meteorological conditions measured at both transect stations ( $z_1, z_2$ ) using a mixing parameter  $m$  as follows:

$$\psi_{(z)}^p = \left(1 - m \frac{z}{z_{LCL}}\right) \psi^s + m \frac{z}{z_{LCL}} \psi^{ML}, \quad (8)$$

Where  $\psi$  is a scalar for potential temperature ( $\theta$ ) or specific humidity ( $q$ ), superscript  $p$  represents the state of the air parcel,  $s$  indicates the conditions at the lowest station used ( $z_1$ ),  $ML$  refers to the mixed-layer, which is an average of conditions observed at the two stations,  $m$  is the mixing parameter ranging from 0 (no mixing) to 1 (maximum mixing), and  $z_{LCL}$  is the height at which LCL is reached. Secondly, to account for the inland effect (observed at  $z_2$  station), LCL is calculated iteratively using an averaged  $\theta$  and  $q$  ( $\psi^{ML}$ ) from  $z_1$  and  $z_2$ . This  $\psi^{ML}$  and LCL are used in Equation 8 to estimate the air parcel state  $\psi_{(z)}^p$ , which is then used to calculate a new LCL. This calculation is repeated several times, with  $\psi^{ML}$  being re-averaged with the conditions at station  $z_2$  in each iteration. This repetitive calculation ensures that the inland conditions ( $z_2$ ) in the MBL's

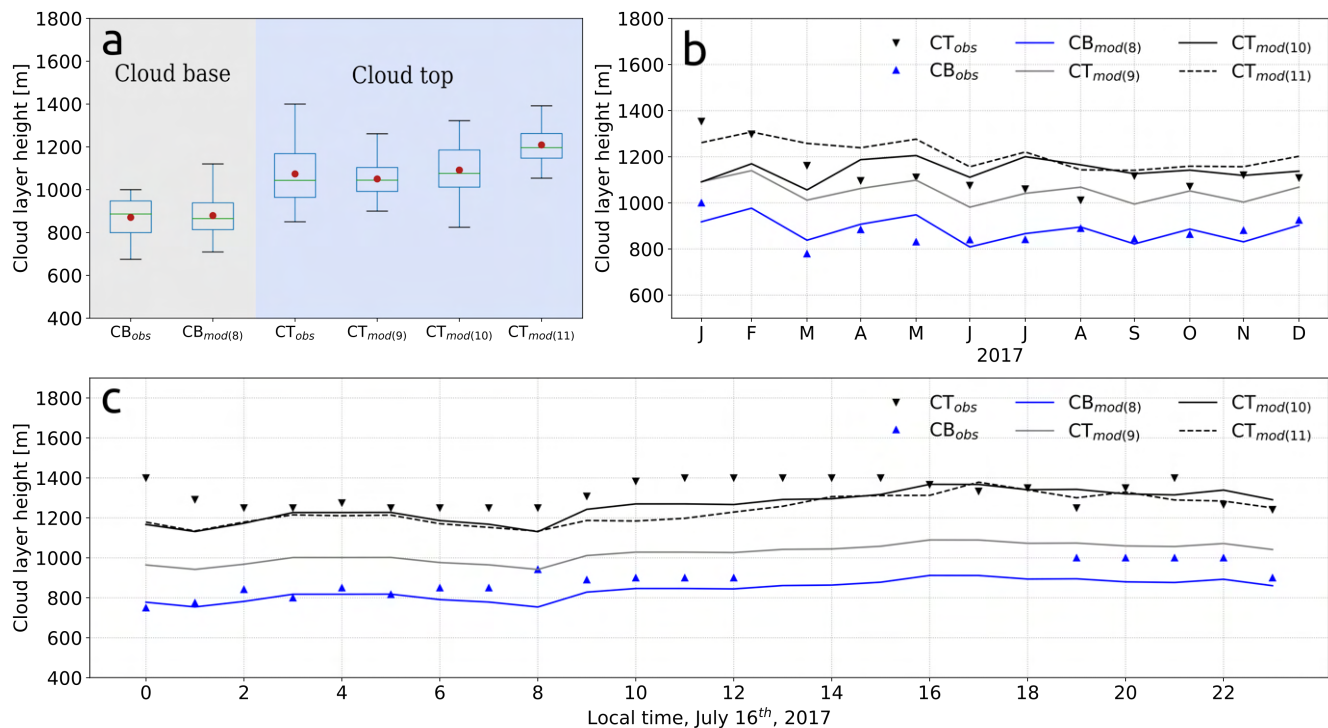


**Figure 4.** (a) Annual, (b) monthly-averaged, and (c) typical diurnal cycle of CB and CT comparisons between observations (obs) and modeling (mod). The subscripts' number refers to the equation number in sections 2.1.2 and 2.1.3.

state are accurately represented. Our estimations show that the appropriate number of iterations is related to the distance in km between  $z_1$  and  $z_2$ . For example, if  $z_1$  and  $z_2$  are separated by 5 km, we iterate five times.

The physical interpretation of this topographic uplifting is depicted in Figure 2b, where the initial iteration represents an equal (averaged) influence of marine ( $z_1$ ) and inland ( $z_2$ ) conditions. Subsequent iterations represent the dominance of inland conditions over marine conditions. Dominant marine conditions exhibit a higher latent heat flux (blue arrow in Fig. 2b) compared to sensible heat flux (orange arrow in Fig. 2b). Conversely, inland-dominant conditions showcase a prevalence of sensible heat flux over latent heat flux (Fig. 2b). The shift in surface energy partitioning toward dominant sensible heat flux (inland conditions) leads to the LCL being reached at a higher altitude, resulting in the uplifting of the Sc cloud (Fig. 2c). This phenomenon is due to the warmer and drier conditions prevalent over land. It is important to note that during the advection of the Sc cloud, the MBL remains well-mixed, thereby minimizing differences between marine ( $z_1$ ) and inland conditions ( $z_2$ ).

To assess the accuracy of our CB estimations, Figure 4 presents a multi-temporal comparison between CB estimations derived from the AMARU model and observations conducted in the Atacama Desert in 2017 as part of the Ground Optical Fog Observations (GOFOS) experiment (del Río et al., 2021a). The GOFOS experiment entails year-long monitoring of cloud base and top dynamics during an ENSO-neutral year (2017), employing optical cameras placed across the terrain to record

205 the vertical movement of Sc cloud and fog. The left panel of Figure 4a illustrates that CB estimates generated by the model using Equation 8 ( $CB_{mod(8)}$ ) closely align with those observed in 2017. The mean values of the estimated CB stand at 879 m compared to the observed average of 870 m, with similar standard deviations of 88 m and 93 m, respectively. This satisfactory performance of the model in estimating CB is also observed on a monthly scale in Figure 4b, where the estimated CB generally differs by  $\sim 50$  m from the observed values on a monthly basis. To assess the model's capacity to replicate the diurnal cycle of CB, Figure 4c shows a representative foggy day in the Atacama region. It is evident from the figure that the estimated CB closely tracks its diurnal cycle, with errors of  $\sim 100$  m observed during the afternoon.

### 2.1.3 Cloud Top, CT

The parcel method, upon which our CB calculations are founded, determines  $r_l$  from the LCL level upward, according to atmospheric pressure decreases. However, atmospheric pressure also decreases beyond the MBL, where the Sc stands. Consequently, it becomes necessary to estimate the Cloud Top (CT [m]) in order to calculate the  $r_l$  within the cloud layer. Given 215 the challenges associated with estimating CT using basic meteorological data and taking advantage of the homogeneity of Sc as a cloud layer, we propose estimating CT as the function of modeled CB using three simple linear regression models. These models are phenomenological expressions based on CT measurements obtained during the GOFOS experiment in 2017 (del Río et al., 2021a). The proposed linear regression models are as follows:

$$220 \quad CT_{mod(9)} = 236.47 + 0.9355(CB) \quad (9)$$

$$CT_{mod(10)} = CB + CB \sqrt{\frac{FF}{2}} \quad (10)$$

$$CT_{mod(11)} = 236.47 + 0.9355(CB) \left(1 - \frac{\partial\theta}{\partial z}\right) 100 \quad (11)$$

Equation 9 shows a linear regression model in which CT [m] solely depends on CB [m], where constants are determined from the relation between observed CB and CT during the GOFOS experiment. Equations 10 and 11 correspond to linear 225 regression models where CT is determined by CB and fog frequency. The FF (fog frequency [%], section 2.1.1.) in Equation 10 and the vertical potential temperature gradient ( $\partial\theta/\partial z$  [K m<sup>-1</sup>], Fig. 3a) in Equation 11 are based on observations conducted during the GOFOS experiment, where CT demonstrates a negative correlation with fog frequency (del Río et al., 2021a). A comparable linear regression model, combining CB and fog frequency to estimate CT, has been tested in various locations within the coastal Atacama region by Lobos-Roco et al. (2024).

230 Figure 4 shows the effectiveness of linear regression models in predicting CT compared to observations obtained from the GOFOS experiment. The right panel of Figure 4a shows the performance of the three linear regression models against observations for the year 2017. The annual means of the three models are similar to the observed value of (1073 m), with respective values of 1050 m, 1091 m, and 1209 m. However, the CT derived from Equation 10 is the one that performs better, exhibiting a standard deviation of 142 m compared to the observed value of 124 m. At the monthly scale (Fig. 4b), the CT estimated by  
 235 Equation 11 overestimates observations by 150 m. However, the CT derived from equations 9 and 10 remains within a 50 m range of the observed values. In Figure 4c, showing a representative diurnal cycle during the foggy season, both observed and modeled CTs are presented. Here, it is evident that the CT estimated by equations 10 and 11 demonstrates better performance, closely aligning with observations (black triangles). However, the CT estimated from Equation 9 underestimates observations by over 200 m. These three linear regression models offer a statistical framework for estimating CT, with performance varying  
 240 based on temporal scale. Henceforth, in this manuscript, we adopt the CT derived from Equation 10.

#### 2.1.4 Liquid Water Mixing Ratio $r_l$

Once estimated fog frequency (FF), the fog Cloud Base (CB), and Cloud Top (CT) using simple meteorological data from a topographic transect, we proceed to determine the adiabatic liquid water mixing ratio  $r_l$  ( $\text{g kg}^{-1}$ ) within the cloud layer ( $z$ : CT-CB). To achieve this, we utilize the following equation:

$$245 \quad r_l(z) = r_v(z) - r_s(z); r_l \geq 0 \quad (12)$$

where  $r_v$  is the mixing ratio between grams of mass water vapor over a kilogram of dry air,  $r_s$  is the saturated mixing ratio, and  $z$  represents the vertical level between CB and CT (Fig. 2a). Here, since  $r_v$  is very close to be a conserved variable ( $r_v \sim q_v$ ), it is assumed as constant over the cloud layer. Therefore, any excess of  $r_v$  with respect the change of  $r_s$  (T) will result in  $r_l$ . It is important to note that, using a combination of stations  $z_1$  and  $z_2$  as in Equation 8, the term  $r_v$  is assumed as the specific  
 250 humidity of the mixed MBL ( $q^{ML}$ ), and  $r_s$  depends on absolute temperature, therefore it is influenced by  $\theta^{ML}$ .

Figures 5a and 5b show the validation of the model-estimated adiabatic liquid water mixing ratio ( $r_l$ ) against observations of liquid water content (LWC) (CLU, 2024) derived from combined measurements of a microwave radiometer with a Doppler lidar (Schween et al., 2022), conducted at the Diego Aracena Airport in the coastal Atacama Desert during July 2018.

In general terms, Figures 5a and 5b show a satisfactory comparison between our modeled estimations of liquid water content  
 255 and the measured ones. The mean observed values peak at  $0.1 \text{ g m}^{-3}$  at 800 m altitude, while our mean estimations peak at  $0.09 \text{ g m}^{-3}$  at the same altitude ( $\sim 800 \text{ m}$ ), consistent with typical values found in marine Sc clouds. When analyzing the 0.95 percentile curve (red line in Fig. 5) the model follows the vertical distribution of observations, exhibiting peaks of  $0.7 \text{ g m}^{-3}$  between 700 and 900 m ASL when observation shows peaks of  $0.5 \text{ g m}^{-3}$ . Upon comparing the model and observations percentile 0.95, we observe that the model overestimates observations by  $\sim 0.2$  to  $0.3 \text{ g m}^{-3}$ . Finally, upon integrating the  
 260 vertical column of LWC, we also observe similarities in the mean liquid water path (LWP) with values of  $3.6 \text{ g m}^{-2}$  and

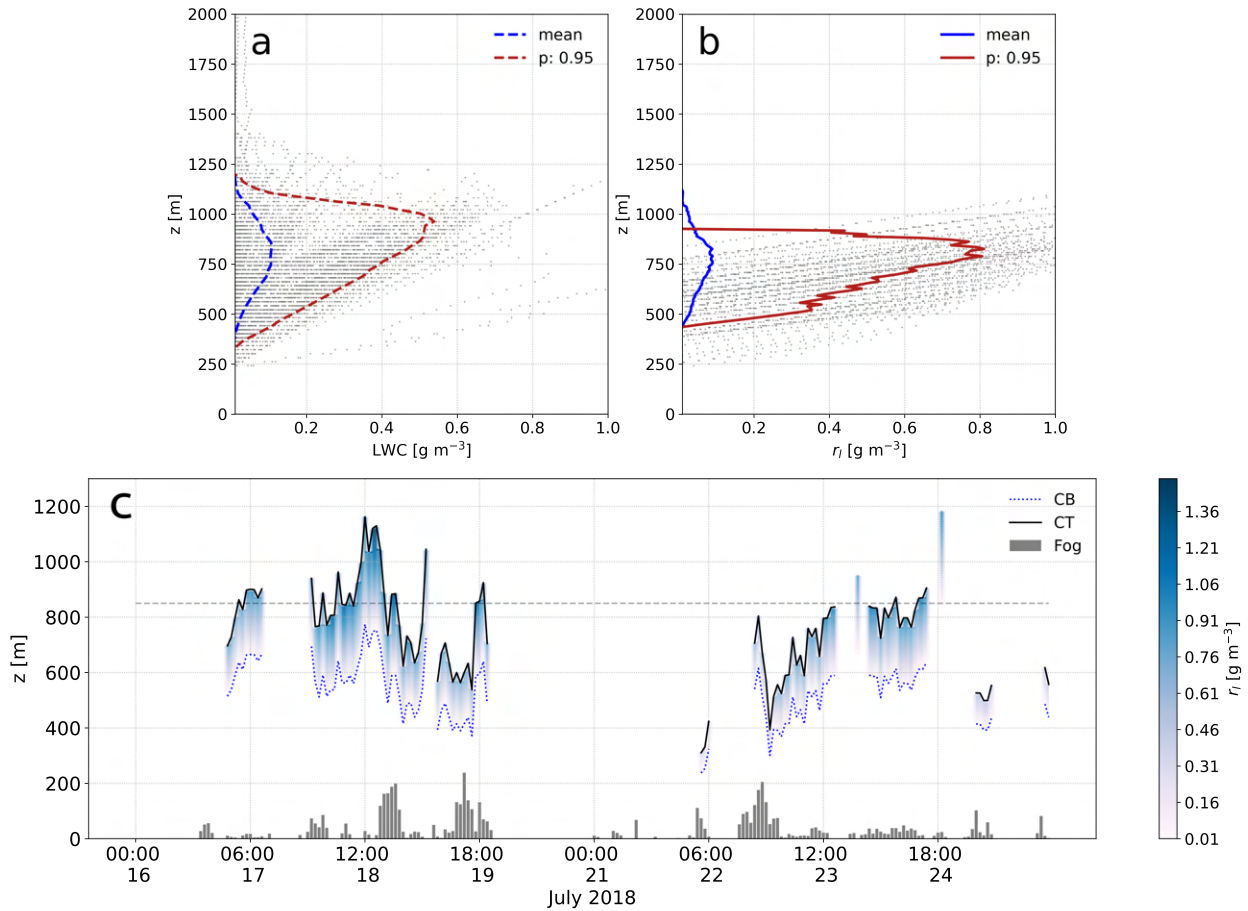


**Figure 5.** Vertical profiles of  $r_l$  (in  $\text{g m}^{-3}$ ) (a) derived from a microwave radiometer and Doppler lidar observations (Schween et al., 2022; CLU, 2024) and (b) estimated by the AMARU model over Diego Aracena Airport. Grey dots represent hourly-averaged profiles filtered by the 0.99 percentile; red lines represent the 0.95 percentile, and the blue line represents the mean. (c) The evolution of the vertical profile simulated by the AMARU model for the Alto Patache Site. Grey bars at the bottom represent fog collection measurements at 850 m (dashed line).

2.6 kg m<sup>-2</sup> for modeled and observed data, respectively. To validate the results obtained from the thermodynamic module of the AMARU model, Figure 5c presents the temporal evolution of a simulated fog cloud during a fog event occurring between July 16<sup>th</sup> and 25<sup>th</sup>, 2018, at the Alto Patache site. The figure illustrates the model's capability to accurately represent fog-cloud frequency, its vertical structure, and water density ( $r_l$ ) over time. In terms of fog frequency, our model shows fog-  
 265 cloud formation from the 17<sup>th</sup> to the 19<sup>th</sup> and from the 22<sup>nd</sup> to the 24<sup>th</sup>, aligning with the periods of highest fog collection rates (grey bars). From the 19<sup>th</sup> to the 22<sup>nd</sup>, our model does not depict cloud formations, consistent with near-null fog water collection during this period. Likewise, we observe that changes in the vertical structure of the cloud (base and top) correspond to variations in liquid water content and fog collection.

In summary, our straightforward methodology, employing a topographic transect of meteorological stations, effectively  
 270 estimates the  $r_l$  within the MBL vertical column. This estimation is achieved by combining thermodynamic principles and statistical regressions, supported by climatological observations. Notably, our approach not only provides estimates not only of  $r_l$  but also of fog frequency and the vertical structure of the fog cloud, thus enhancing our understanding of the fog phenomenon in coastal arid regions.

## 2.2 Water potential module: collector efficiency coefficient ( $\eta$ )

275 The second critical parameter in our proposed model is the collector efficiency coefficient ( $\eta$ ). This variable is intricately linked with complex processes and factors such as wind flow, liquid water content, droplet size, collector positioning, material properties, mesh curvature and porosity (Carvajal et al., 2020). To ensure our assumptions align with climatological observations, we determine the collector efficiency using an empirical coefficient. This coefficient, previously defined in Equation 4, is now redefined as the ratio between the observed fog collection ( $f_{obs}$ ) and the fog inflow ( $F_{in}$ ), where  $f_{obs} = W_h$ . As a ratio,  $\eta$  rep-  
 280 represents the percentage of the maximum water that a fog collector can potentially capture under given atmospheric conditions.  $\eta$  is calculated as follows:

$$\eta = \frac{f_{obs}}{F_{in}}. \quad (13)$$

Note that both  $F_{in}$  and  $f_{obs}$  are averaged per hour, therefore both terms have the unit of L m<sup>-2</sup> h<sup>-1</sup>. Since  $\eta$  is calculated based on fog observations, its value depends on the type of collector used, providing flexibility to the model to adapt to different  
 285 collector types if observations are available.

Table 1 shows the empirical collector efficiency coefficient ( $\eta$ ) calculated for five fog collection stations located between 600 and 1200 m along the coastal strip of Chile. Overall, mean  $\eta$  varies from 15% to 27%, with variability ranging from 4% to 45%. Three factors contribute to this variability in the efficiency coefficient. Firstly, the model's ability to accurately determine fog frequency (RMSE of 6% in Fig. 3a) can lead to discrepancies, potentially resulting in very high ( $\eta \sim 100\%$ ) or null ( $\eta \sim 0\%$ )  
 290 efficiencies when fog collection is observed, thus altering the averages. Secondly, wind speed may also play a significant role, as it is responsible for transporting  $r_l$  through the collector. Lastly, both the material of the mesh and its curvature during fog

Coordinate	Altitude	Time period	mean	25%	50%	75%
19.17° S- 70.17° W	850 m	2022	16%	5%	13%	26%
20.48° S- 70.05° W	1200 m	2019	26%	6%	16%	30%
20.82° S- 70.14° W	850 m	2018	24%	11%	19%	31%
30.65° S- 71.68° W	630 m	2022	27%	6%	20%	45%
32.16° S- 71.49° W	650 m	2022	15%	4%	5%	21%

**Table 1.** Descriptive statistics of the empirical efficiency coefficient  $\eta$  estimated at five fog collection stations along a 2000 km coastal strip in Chile.

collection could impact mesh efficiency (Carvajal et al., 2020). Despite the variability in  $\eta$  across all sites, we find an average efficiency coefficient of  $25\% \pm 10\%$ , consistent with results in the literature. For instance, Montecinos et al. (2018) reported efficiencies ranging from 0% to 36% in large fog collectors. Similarly, using numerical simulations, Carvajal et al. (2020) reported a mean efficiency of 28% with a theoretical maximum of 36%. Finally, de Dios Rivera (2011) reported maximum fog collection efficiencies between 20% and 24% using a simple numerical model approach for different mesh types.

For our study, we use an  $\eta$  of 0.25 (25%). Once  $\eta$  is estimated, we can readily solve Equation (6) to obtain an estimation of fog water harvesting ( $W_h$ ). Given that  $r_l$  has a vertical dimension, assuming a constant wind speed ( $u$ ) along the MBL, we can derive the vertical distribution of fog harvesting.

### 2.3 Spatial module: fog harvesting maps

In addition to the thermodynamic module, we propose a spatial module for extrapolating the vertical variability of  $W_h$  into a horizontal spatial domain. To do this, we integrate the vertical domain ( $z$ ) of  $W_h$  to an area of optimal fog harvesting potential obtained from a combination of a digital elevation model (DEM) and GOES satellite images. We outline four steps to achieve this spatial variability.

The first step involves reclassifying the DEM grid cells based on the cloud layer height and removing all grid cells below the CB and above the CT elevation. This reclassification ensures that only the elevation range where the Sc cloud could potentially impact the topography is considered. In the second step, we create an aspect image (slope orientation) with the DEM and reclassify the pixels based on the angle range of the main wind direction (mean  $\pm$  std) when fog is collected (obtained from observations at the  $z_2$  station). The third step involves calculating the fog and low cloud (FLC) frequency using data from the GOES satellite (del Río et al., 2021b; Espinoza et al., 2024). This algorithm continuously calculates the presence and absence of FCL in every GOES grid cell. The third step serves as a geographical framework, delineating the area where fog-cloud interacts with topography. The spatial intersection of the three steps generates optimal areas for fog collection, physically representing the locations where the Sc cloud and its harvesting potential intersect the surface. It is important to note that the values of grid cells in these optimal areas for fog collection represent elevations (m ASL) in areas with high FLC frequency. The final step involves replacing the elevation grid cell values of the optimal fog collection areas with the vertical distribution of potential

fog harvesting ( $W_h$ ). As  $W_h$  values are associated with a vertical domain ( $z$ ), each  $W_h$  value can be mapped onto the resulting grid of optimal fog collection areas. The result of this last step yields a spatial distribution of potential fog harvesting.

### 3 Model applications to (semi-)arid study case sites

The AMARU enables us to evaluate the spatiotemporal variability of fog harvesting using routine meteorological data and satellite products. In this section, we evaluate the application of the model ( $W_h$ ) at three sites along the coastal strip of Chile, corresponding to hyper-arid, arid, and semi-arid ecosystems between 2018 and 2023.

Figure 6 shows the geographical setting of the study sites, which correspond to hyperarid (Site a), arid (Site b), and semi-arid (Site c) fog ecosystems situated between 600 and 1200 m ASL along the coastal mountains of Chile. Generally, these sites represent xeric ecosystems (Muñoz-Schick et al., 2001) sustained year-round by fog, with a frequency exceeding 40% (Fig. 6). Each of these three sites is equipped with meteorological and fog collection instrumentation, managed by the Centro UC Desierto de Atacama of Pontificia Universidad Católica de Chile. The characteristics of these stations and their data and parameters used in the model are summarized in Table 2. In addition, to meet the model's requirements, observations from these three sites ( $z_2$ ) are complemented with data from near-sea level observations ( $z_1$ ), sourced from public datasets (www.agromet.cl), which are also detailed in Table 2.

Site	Coordinates	Height	Distance coast	$\eta$	Available data	Time period
$a_{z_2}$	20.82° S-70.14° W	850 m	5 km	25%	T, RH, P, U, WD, fog collection	01-01-2018
$a_{z_1}$	20.52° S-70.15° W	48 m	1 km		T, RH, P, U, WD	31-12-2018
$b_{z_2}$	26.00° S-70.60° W	820 m	2 km	25%	T, RH, P, U, WD, fog collection	01-05-2023
$b_{z_1}$	26.29° S-70.62° W	120 m	2 km		T, RH, P, U, WD	31-10-2023
$c_{z_2}$	32.16° S-71.49° W	650 m	3 km	25%	T, RH, P, U, WD, fog collection	01-09-2022
$c_{z_1}$	32.16° S-71.51° W	60 m	1 km		T, RH, P, U, WD	31-12-2022

**Table 2.** Geographic characteristics and available data of observational sites ( $z_2$ ) and their corresponding stations at the coast ( $z_1$ ).  $T$  represents air temperature at 2 m,  $RH$  relative humidity,  $P$  air pressure,  $U$  wind speed, and  $WD$  wind direction.

#### 3.1 Seasonal cycle of modeled and observed fog harvesting

AMARU satisfactorily reproduces the observations of fog harvesting in both magnitude and variability over time. Figure 7 shows a comparison of monthly-average daily rates of fog harvesting at the three analyzed sites. Overall, the model results (blue) follow the seasonal cycle of observed fog collection (grey) across latitudes, albeit showing annual disagreements with observations by 0.5 to 1  $L m^{-2} d^{-1}$ . In the hyperarid environment of Site (a) (Fig. 7a), the model estimates an annual daily rate of 5.0  $L m^{-2} d^{-1}$ , which satisfactorily compares to the rate of 5.5  $L m^{-2} d^{-1}$  obtained through observations. Likewise, the model can closely track the seasonal cycle of fog harvesting, exhibiting low rates in summer (January to March) and autumn (April to June) and higher rates in winter (July to September) and spring (October to December). Moreover, the model correctly



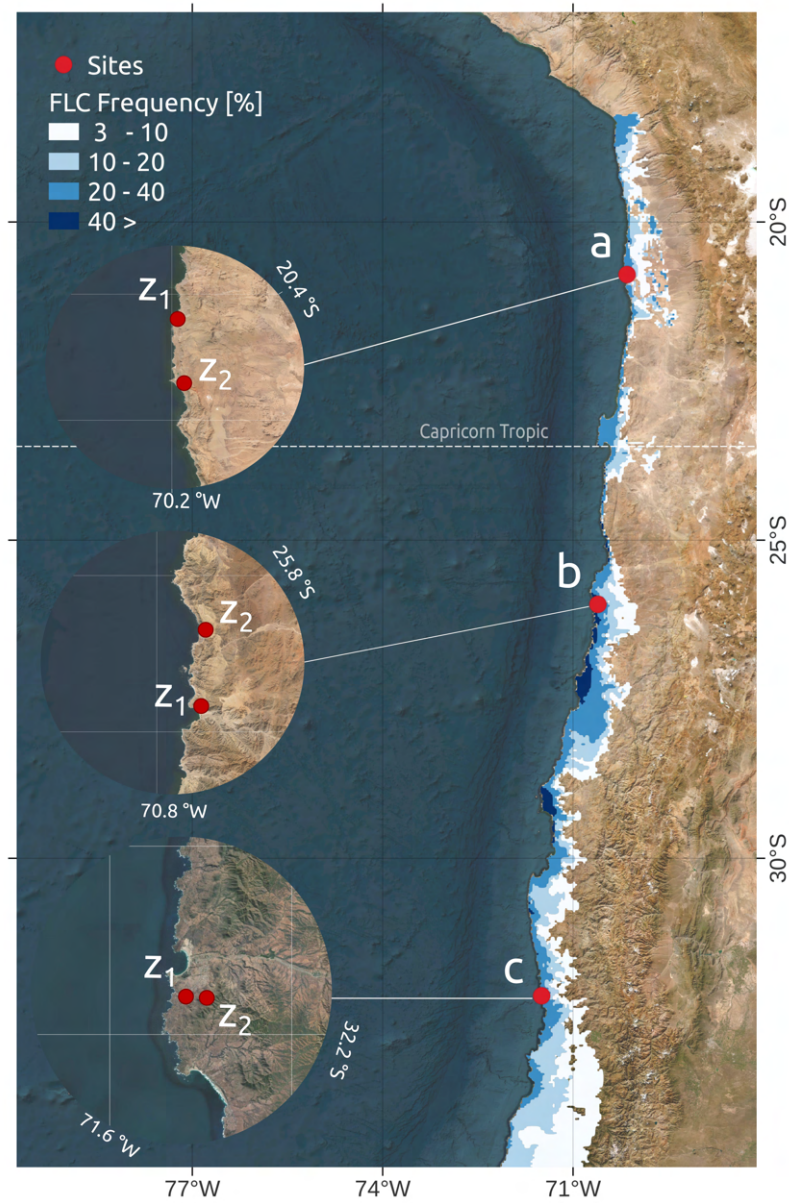


**Figure 6.** Location of the study sites and their meteorological stations. The blue-coloured areas represent the fog and low cloud (FLC) frequency obtained by the GOES satellite (del Río et al., 2021b) between 2018 and 2023.  $z_1$  and  $z_2$  represent the meteorological stations forming the transect used for running the model according to our methodology.

estimates the frequency of fog events. For instance, during summer, the model estimates a very low (January and March) or null (February) fog collection, with mean errors around  $0.39 \text{ L m}^{-2} \text{ d}^{-1}$  in the season compared to observations. Similarly, during the optimal fog harvesting season between winter and spring, the model correctly estimates the monthly magnitude of observed fog collection with errors of  $2 \text{ L m}^{-2} \text{ d}^{-1}$ . Finally, the model successfully replicates the variability in the monthly daily rates of fog collection as indicated by the error bars in Figure 7. For example, in spring at Site (a), the observed mean variability rates (errors bars) range from 4 to  $9 \text{ L m}^{-2} \text{ d}^{-1}$ , while the model estimates spring mean rates ranging from 6 to  $10 \text{ L m}^{-2} \text{ d}^{-1}$ .

For Site (b), situated in an arid environment (Fig. 6), the amount of fog collection is notably lower compared to Site (a) (hyperarid). However, the model accurately reproduces the annual-averaged daily rate of fog harvesting of  $4.3 \text{ L m}^{-2} \text{ d}^{-1}$ . Despite this overall good performance, the model still underestimates observations by approximately  $1 \text{ L m}^{-2} \text{ d}^{-1}$  during winter in terms of magnitude and variability (as indicated by the error bars). Unfortunately, the annual cycle for Site (b) remains incomplete as observations were only recorded from May to October 2023. For the semi-arid environment of Site (c) the model shows annual daily rates of fog harvesting similar to those of Site (b), albeit with an overestimation of  $1 \text{ L m}^{-2} \text{ d}^{-1}$  compared to observations. During the months with the highest fog collection rates (September to December), the model overestimates observations in average by  $\sim 0.7 \text{ L m}^{-2} \text{ d}^{-1}$ . It is worth mentioning that these discrepancies in estimation are not systematic, and despite them, the model captures the same seasonal cycle obtained through observations at all three sites.

### 3.2 Vertical variability of fog harvesting potential ( $W_h$ )

Since the model estimates the liquid water content ( $r_l$ ) in the vertical column of the Sc cloud when it interacts with topography, and assuming constant wind at  $z_2$  throughout the vertical, we can model the fog harvesting potential at every height within the Sc cloud layer.

Figure 8 shows the vertical variability of  $W_h$  potential for the three analyzed sites. In the figure, dots represent the total  $W_h$  per hour at each height within the fog-cloud layer over the course of one year. The red line depicts the annual average daily rate of  $W_h$  as a function of height, while the black dot shows the observed annual average daily rate. In addition, the dots are colour-coded based on the corresponding  $r_l$  values. From Figure 8, it is evident that fog harvesting potential decreases from the hyperarid (north) to the semi-arid (south) regions for both  $W_h$  and  $r_l$ . Specifically, in the hyperarid site, a  $W_h$  of  $10 \text{ L m}^{-2} \text{ d}^{-1}$  can be easily reached, whereas in the arid and semi-arid sites, maximum  $W_h$  of 5 and  $3 \text{ L m}^{-2} \text{ d}^{-1}$ , respectively, are observed. The same behaviour is observed for  $r_l$ , which exhibits higher values (mean percentile 0.95 up to  $0.7 \text{ g kg}^{-1}$ ) in the hyperarid site compared to the arid and semi-arid sites, where percentile 0.95 percentile reaches up to  $0.6 \text{ g kg}^{-1}$  and  $0.4 \text{ g kg}^{-1}$ , respectively. The vertical variability of  $W_h$  also allows us to study the vertical liquid water capacity of the fog cloud. For instance, in the hyperarid site, the model estimates fog harvesting potential from 600 m up to 1350, while in the arid and semi-arid sites, fog can be harvested from 500 to 1250 and from 370 to 1050, respectively. These variations in  $r_l$  and the fog cloud layer height are explained in Equation (3) and Figures 2b and 2c. In Equation (3), we show that the calculation of cloud base, and consequently  $r_l$ , is influenced by the combined conditions of stations  $z_1$  and  $z_2$ . For example, in the hyperarid site situated within the tropics (Fig. 6), air temperature is higher at both  $z_1$  and  $z_2$  compared to the semi-arid site. This implies

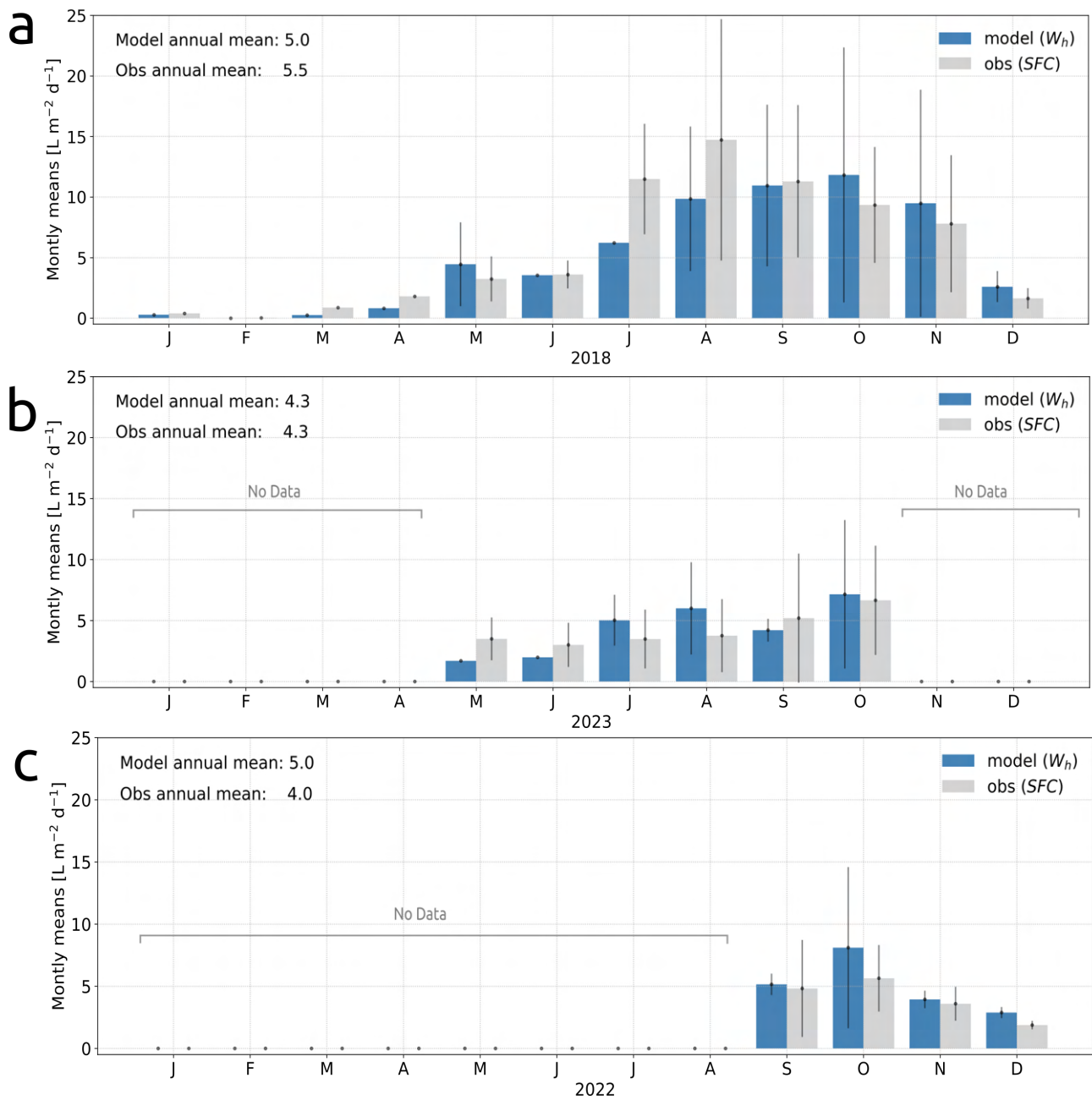


**Figure 7.** Comparison of monthly-averaged daily fog collection rates between model (blue) and observations (grey) in three fog ecosystems situated on the (a) hyperarid, (b) arid, and (c) semi-arid Chilean coast. The error bars show data variability between the 25<sup>th</sup> and 75<sup>th</sup> percentiles.

that the condensation of the air parcel in Site (a) will occur at a higher altitude than in Site (b). Likewise, higher temperatures increase the air's capacity to hold humidity, resulting in a higher  $r_l$  observed in the hyperarid site compared to the semi-arid one. Another significant factor contributing to the difference in  $r_l$  and cloud layer height is the distance from the coast at which station  $z_2$  is located. For instance, the hyperarid site is 5 km inland compared to the arid and semi-arid sites located 2 km and 3 km away from the coast, respectively (Table 2). Consequently, inland conditions in the hyperarid site are hotter than in the other two sites, contributing to the formation of the cloud layer at higher altitudes.

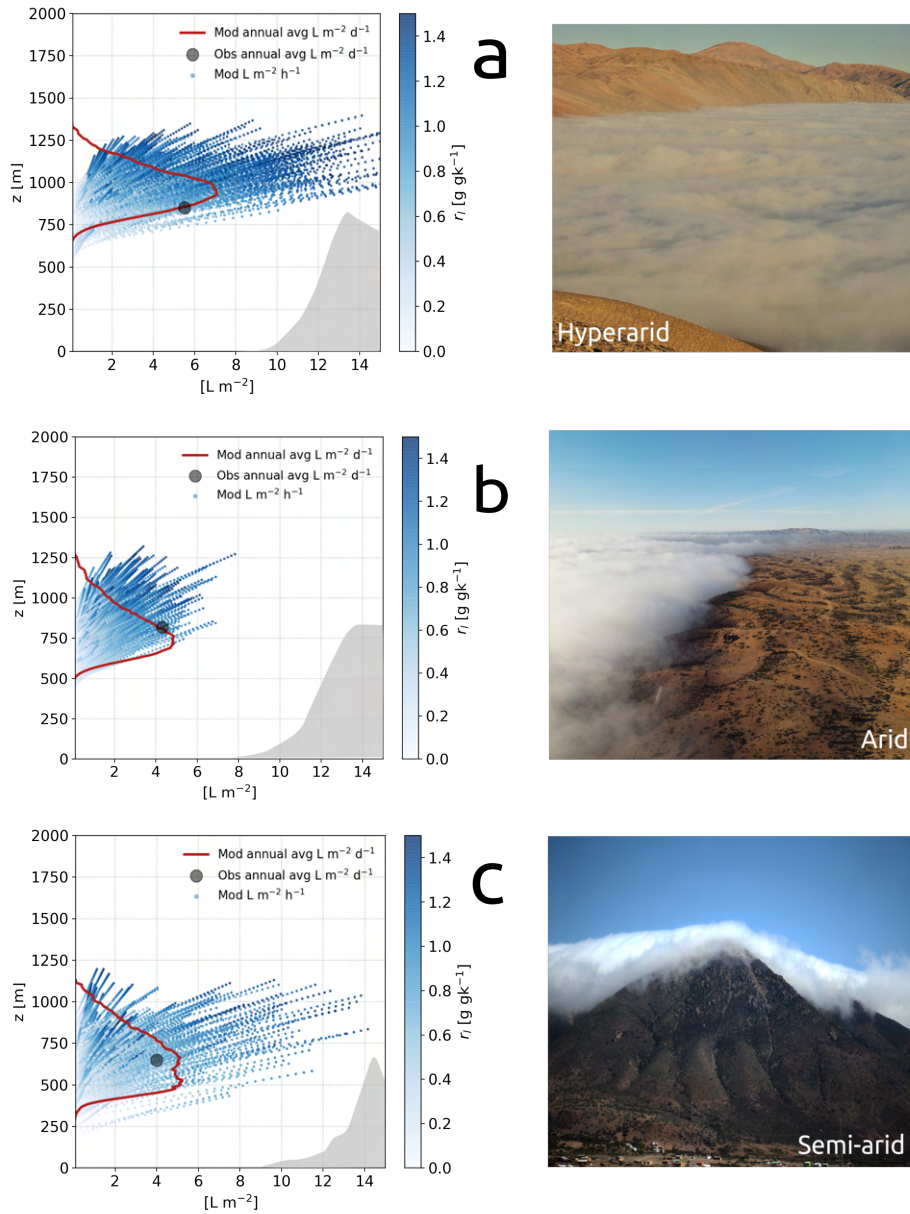
Figure 8 also shows the annual average daily rates (red line) estimated by the model and observed by a standard fog collector (black dot). This red line indicates the vertical placement of the maximum annual  $W_h$ . For example, in the hyperarid site, the maximum  $W_h$  is located at 900 m in height, while observations are situated at 850 m ASL, explaining the highest annual daily fog collection rates. In contrast, in the arid and semi-arid sites, the maximum  $W_h$  is not aligned with the height of the observations. For Site (b), the maximum  $W_h$  is reached at  $\sim 680$  m, whereas observations are located at 820 m ASL. Similarly, for Site (c), the maximum  $W_h$  is situated at 500 m, while observations are at 650 m ALS. The validation of annual average daily rates in Figure 8 is determined by the proximity of the black dot to the red line at the observed height. For example, in Figure 8a, we observe an underestimation by the model, which is also evident in Fig 7a, though not in the vertical dimension, as the observations differ by  $\sim 0.5 \text{ L m}^{-2} \text{ d}^{-1}$  from the modeling results. For sites (b) and (c) (Figs. 8b and 8c), the model accurately reproduces the annual daily rates, consistent with the observation, as also observed in Figures 7b and 7c.

### 3.3 Spatial variability of $W_h$ : fog harvesting potential mapping

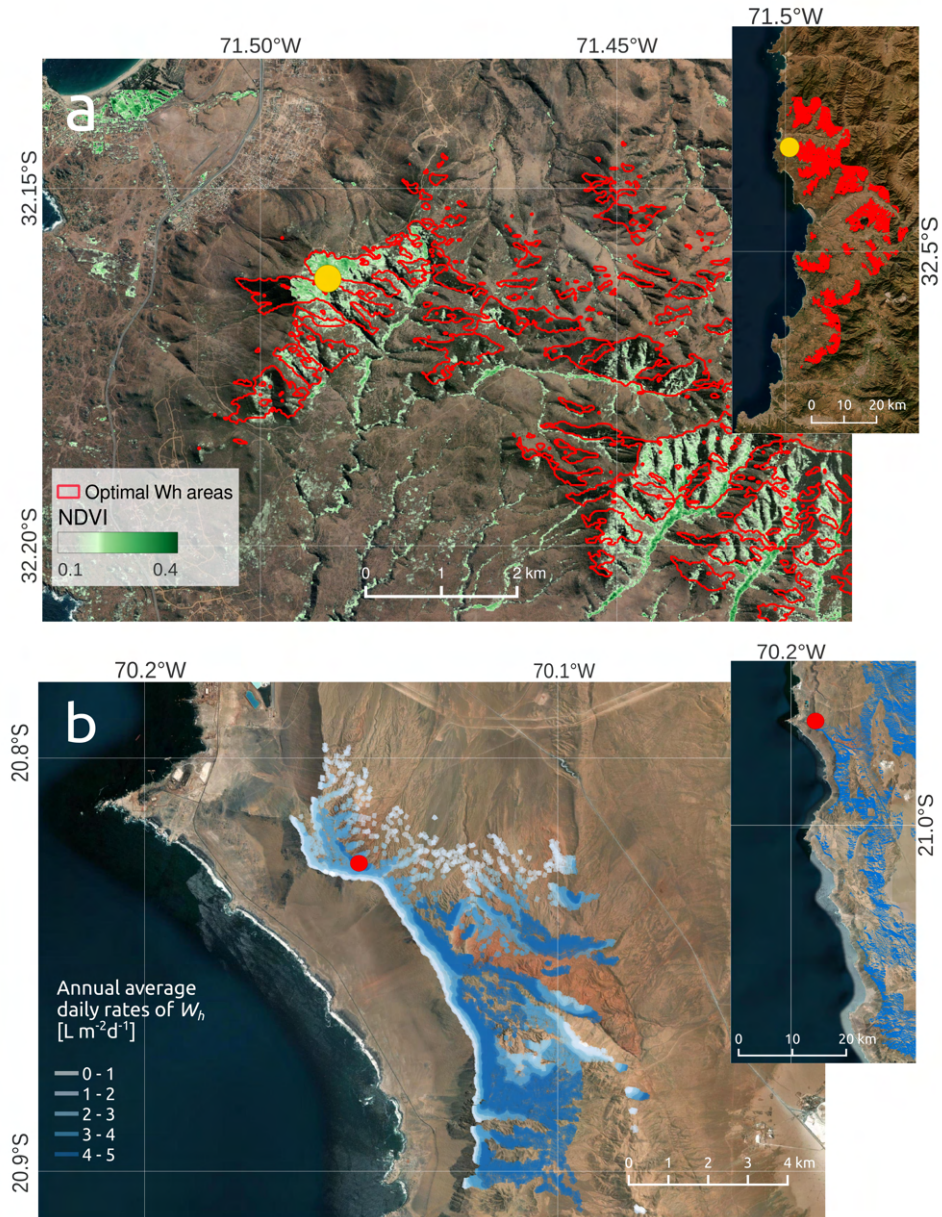
The combination of AMARU's results with satellite products enables us to interpolate the influence of the Sc cloud over land and its potential harvesting in space. This subsection introduces two examples of AMARU's results in spatial variability that can be utilized for fog ecosystem delimitation and water planning.

Figure 9a shows the optimal fog harvesting areas highlighted in red, corresponding to the region where the Sc cloud interacts with the Earth's surface. For Site (c), these areas are displayed near the summit of the coastal mountains, specifically ranging from 370 m to 1050 m ASL (Fig. 8c). In addition, based on data from the meteorological Station ( $z_2$ ) at this site, the fog cloud flux originates from the South and Southeast ( $110^\circ$  to  $300^\circ$ ), which is reflected in the model's depiction of the mountain slopes facing South and Southeast. In the zoomed-out view of Figure 9a, we observe that the extent of these optimal fog harvesting areas spans within the first  $\sim 20$  km from the coast, as determined by the frequency of fog and low clouds derived from the GOES satellite (section 2.3).

To independently validate the spatial interpolation of AMARU's results, we compare the optimal fog harvesting areas with fog-dependent vegetation. In Figure 9a, areas highlighted in green represent the normalized difference vegetation index (NDVI) estimated through Sentinel satellite imagery. Overall, the optimal fog harvesting areas align with areas exhibiting the highest NDVI values. For example, a concentration of NDVI is observed at the summit of the mountains and the southeast slopes, indicative of a forest ecosystem sustained by fog (Garreaud et al., 2008). Furthermore, NDVI also concentrates at the bottom of small valleys downstream of the summits, suggesting that fog water accumulated on the summits may potentially flow down, supplementing the precipitation input to the streams.



**Figure 8.** Vertical variability of modeled fog harvesting ( $W_h$ ) in the (a) hyperarid, (b) arid, and (c) semi-arid sites. Dispersed dots represent the total fog harvesting at every hour; the red line is the annual average daily rate of  $W_h$ , and the grey dot is the observed annual averaged daily rate of  $W_h$ . The dispersed dots are color-coded on a blue scale representing the liquid water content ( $r_l$ ). The grey shading represents the topographic profile of each site. The right panels show a photograph of each site during a fog event.



**Figure 9.** (a) optimal fog harvesting areas (red line) resulting from the model for Site (c) compared to the normalized difference vegetation index (NDVI, ranging from 0.1 to 0.4) estimated through Sentinel satellite images for 2022. The yellow dot indicates the meteorological station ( $z_2$ ). (b) Spatial variability of annual average daily rates of  $W_h$  for the Site (a) estimated during 2018. The red dot indicates the meteorological station ( $z_2$ ).

Figure 9b shows the spatial variability modeled from the intersection between the vertical profile annual average daily rate (red line, Fig. 8a) and the optimal fog harvesting areas. In the figure, we observe the spatial distribution of the fog water potential along the mountain, with maximum values observed around 900 m. The topography of the mountain favours altitudes around 900 m ASL with Southwest slope orientations, leading the model to project large areas with fog harvesting potential ranging from 4 to 5 L m<sup>-2</sup> d<sup>-1</sup>. In the eastern areas of the meteorological station (red dot,  $z_2$ ), fog harvesting potential decreases to lower altitudes, consistent with results presented in Figure 8a. Likewise, decreases towards the southwest of the station at higher altitudes until it disappears. The area surrounding the station corresponds to the well-known fog oasis of Alto Patache (Muñoz-Schick et al., 2001), situated between 600 and 850 m, within the optimal areas of fog harvesting determined by the model.

This model application is further extrapolated to the entire region to determine optimal fog harvesting spots within the area of influence of fog and low clouds, as determined through the GOES satellite. An example of these larger areas is shown in the zoomed-out view of Figure 9b, where optimal fog harvesting areas are situated within 10 km from the coast. Since the model runs with simple meteorological time series, fog harvesting potential maps can be generated for different time averages, enabling us to study and assess spatial changes in fog harvesting potential over hours (events), days, seasons, and years.

#### 4 Model limitations and challenges

Despite the versatility of the AMARU model in representing the harvesting of the advective fog phenomenon in both time and space, it has several limitations worth describing.

Firstly, one of the most important variables in the model is the adiabatic liquid water mixing ratio ( $r_l$ ), which is estimated assuming water vapor is condensed because it reaches saturation. Despite our simplistic approach and reliable results, we know that further model improvements must be made by including essential microphysical processes. Such processes are mean volume diameter, effective size, droplet concentration, and effective droplet size (Gultepe et al., 2021). To account for these processes, comprehensive observations must be performed to get a complete budget equation allowing us to have more realistic modeling.

Secondly, the model's capability to represent fog harvesting in time is primarily limited by the empirical collector coefficient. However, this coefficient remains constant in the model, resulting in both underestimations and overestimations compared to observations. To improve our estimations of fog harvesting over time, further exploration into the collector efficiency is necessary, incorporating factors such as wind speed, collector material properties, and cloud droplet size into more complex functions.

Thirdly, the model's capability to assess fog harvesting potential in the vertical column of the MBL enables us to evaluate the maximum fog harvesting potential beyond single-point observations. However, this vertical  $W_h$  estimation is contingent upon accurately determining  $r_l$  assuming that wind speed remains consistent at every level of the MBL. Although  $r_l$  estimations align with observations from microwave radiometers, our results must be validated with in-situ observations of liquid water content during fog collection. In addition, relevant physical processes influencing CT, such as dry air entrainment from the

free troposphere, and thermal inversion are not included in its calculation. Instead, CT is statistically estimated, leading to  
440 uncertainties in a variable whose precision is crucial for estimating the maximum  $r_l$  and, consequently,  $W_h$ . Regarding wind  
speed, our assumption of a constant horizontal wind along the MBL is based on the mixed layer theory, which posits that  
scalars such as potential temperature, mixing ratio, and wind speed remain constant if the MBL is well-mixed. However, this  
theory does not consider topography, which may disturb this constant pattern when interacting with MBL winds. To improve  
the model's estimation of  $r_l$  and better  $W_h$  potential, future research must incorporate accurate vertical profile observations of  
445 temperature, mixing ratio, and wind speed.

Finally, the spatial extrapolation of  $W_h$  represents a preliminary approach for fog harvesting potential mapping. This is  
because its accuracy is limited by the availability of spatially distributed meteorological data. We spatially extrapolate the  
conditions determined by the model for the  $z_2$  station to all surrounding areas that share the same geographic conditions.  
Nevertheless, this approach may overestimate several inland locations that meet the geographical characteristics of  $z_2$  but not  
450 the atmospheric ones. Improving this spatial extrapolation of  $W_h$  can be addressed using two approaches. The first one involves  
utilizing gridded meteorological data that allows us to solve Equation (6) at every grid point. Unfortunately, available gridded  
data is often too coarse to accurately represent the sub-kilometer fog harvesting phenomenon. The second approach entails  
incorporating the FLC frequency determined by the GOES satellite (Fig. 6) into the spatial interpolation of  $W_h$ . For example,  
we can modify  $W_h$  spatially using a function based on the FLC frequency, where locations with similar geographical conditions  
455 to  $z_2$  station may see their  $W_h$  reduced (increased) if their FLC frequency is higher (lower) than that observed at  $z_2$  station.

## 5 Conclusions

We propose, formulate, and evaluate an observation-driven model, named AMARU, for estimating advective fog water po-  
tential harvesting in (semi-)arid regions. This model uses standard and routine meteorological observations to estimate where,  
when, and how much water can be potentially harvested from fog clouds. The proposed model employs a thermodynamic  
460 approach to estimate fog's adiabatic liquid water mixing ratio, incorporating key physical processes associated with the inter-  
action between the stratocumulus cloud and topography. This approach yields vertical profiles of liquid water mixing ratio,  
from which fog frequency, cloud base, and cloud top can be derived. In addition, by integrating the estimations of liquid water  
mixing ratio with climatological records of fog harvesting observations, we derive an empirical collector efficiency coefficient  
to estimate vertical profiles of potential fog harvesting. Finally, by combining vertical profiles of fog harvesting potential with  
465 satellite products, we introduce a methodology for spatially extrapolating these results, thereby generating fog harvesting po-  
tential maps.

Below, we outline the main conclusions of our research.

- 470 – Despite the simple approach, this model correctly reproduces essential physical components involved in fog harvesting.  
Our model evaluation against available observations shows that model results reproduce: fog frequency (R: 0.95; RMSE:



6%), cloud base and top height (errors <50 m), liquid water content (errors  $\sim 0.2 \text{ g m}^{-3}$ ), and fog collector efficiency (errors  $\sim 5\%$ ). Overall, fog harvesting observations are satisfactorily reproduced by the model with mean errors of 10% ( $< 1 \text{ L m}^{-2}$ ).

- 475 – The simple approach takes advantage of using routine meteorological data, which is widely available worldwide in areas characterized by land-ocean contrast and complex topography.
- However, the model presents several limitations, whose improvement will depend on comprehensive observations and further research. Between the limitations, microphysics observations of cloud droplet size, concentration, and actual water content must be incorporated to improve the model. Moreover, further research must be done on the empirical
- 480 coefficient, which is constant in the model. However, our observations suggest a variability which depends mainly on wind speed, but also on the materials. Finally, future research should incorporate accurate vertical profiles of temperature, mixing ratio, and wind speed to corroborate our vertical modeling assumptions.
- Our model offers a versatile approach with multiple applications in massive fog harvesting planning and ecosystem delimitation for conservation purposes, among others. Since fog is a global meteorological phenomenon, this model holds
- 485 potential for applicability in many coastal (semi-)arid regions, addressing data deficiencies in regions where fog harvesting represents a viable water source.

Finally, we expect this research to yield significant social benefits by providing decision-makers with valuable insights into new water sources, thus aiding in the mitigation of climate change impacts.

490 *Data availability.* <https://data.mendeley.com/datasets/jyk8v2mrhd/1>

*Author contributions.* **Felipe Lobos-Roco:** Conceptualization, Methodology, Software, Writing-Original draft preparation, Data curation, Visualization, Formal Analysis, Writing-Reviewing and Editing, Funding acquisition. **Jordi Vilà Gerau-de Arellano:** Conceptualization, Formal Analysis, Writing-Original draft preparation, Writing-Reviewing and Editing. **Camilo del Río:** Investigation, Conceptualization, and Resources.

495 *Competing interests.* The authors declare that they have no conflict of interest

*Acknowledgements.* This research was funded by CMPC contract n. 6496162. We acknowledge Centro UC Desierto de Atacama for providing data, discussions, and pictures. FL-R acknowledges FONDECYT project no. 1211846 for providing valuable data. Likewise, we

acknowledge Cristobal Merino, Valentina Pacheco, Sebastian Vicuña, and Diego Ibarra for their help in standardizing databases. Moreover, we thank Nicolas Valdivia for photograph B in Figure 8 and the web site: <https://www.davidnoticias.cl/cerro-santa-ines-los-vilos-se-declara-santuario-la-naturaleza/> for photograph C in Figure 8. Finally, we acknowledge E. Fiorin for her English language editing, and Peter Taylor and an anonymous reviewer for their valuable contribution.

## References

- Andersen, H., Cermak, J., Fuchs, J., Knippertz, P., Gaetani, M., Quinting, J., Sippel, S., and Vogt, R.: Synoptic-scale controls of fog and low-cloud variability in the Namib Desert, *Atmospheric Chemistry and Physics*, 20, 3415–3438, 2020.
- 505 Baguskas, S. A., Oliphant, A. J., Clemesha, R. E., and Loik, M. E.: Water and light-use efficiency are enhanced under summer coastal fog in a California agricultural system, *Journal of Geophysical Research: Biogeosciences*, 126, e2020JG006193, 2021.
- Berbel, J. and Esteban, E.: Droughts as a catalyst for water policy change. Analysis of Spain, Australia (MDB), and California, *Global Environmental Change*, 58, 101969, 2019.
- Bergot, T.: Large-eddy simulation study of the dissipation of radiation fog, *Quarterly Journal of the Royal Meteorological Society*, 142, 1029–1040, 2016.
- 510 Carvajal, D., Silva-Llanca, L., Larraguibel, D., and González, B.: On the aerodynamic fog collection efficiency of fog water collectors via three-dimensional numerical simulations, *Atmospheric Research*, 245, 105123, 2020.
- Cereceda, P., Osses, P., Larrain, H., Farias, M., Lagos, M., Pinto, R., and Schemenauer, R.: Advective, orographic and radiation fog in the Tarapacá region, Chile, *Atmospheric Research*, 64, 261–271, 2002.
- 515 Cereceda, P., Larrain, H., Osses, P., Farias, M., and Egaña, I.: The spatial and temporal variability of fog and its relation to fog oases in the Atacama Desert, Chile, *Atmospheric Research*, 87, 312–323, 2008.
- CLU: Custom collection of liquid water content data from Iquique between 9 and 31 Jul 2018, Tech. rep., Cloud remote sensing data centre unit (CLU), [Online; accessed 2024-01-05], 2024.
- de Dios Rivera, J.: Aerodynamic collection efficiency of fog water collectors, *Atmospheric Research*, 102, 335–342, 2011.
- 520 del Río, C., Lobos-Roco, F., Siegmund, A., Tejos, C., Osses, P., Huaman, Z., Meneses, J. P., and García, J.-L.: GOFOS, ground optical fog observation system for monitoring the vertical stratocumulus-fog cloud distribution in the coast of the Atacama Desert, Chile, *Journal of Hydrology*, 597, 126190, 2021a.
- del Río, C., Lobos-Roco, F., Siegmund, A., Tejos, C., Osses, P., Huaman, Z., Meneses, J. P., and García, J.-L.: GOFOS, ground optical fog observation system for monitoring the vertical stratocumulus-fog cloud distribution in the coast of the Atacama Desert, Chile, *Journal of Hydrology*, 597, 126190, 2021b.
- 525 Espinoza, V., Lobos-Roco, F., and del Río, C.: Synoptic control of the spatiotemporal variability of fog and low clouds under ENSO phenomena along the Chilean coast (17°–36° S), *Atmospheric Research*, p. 107533, 2024.
- Estrela, M. J., Valiente, J. A., Corell, D., Fuentes, D., and Valdecantos, A.: Prospective use of collected fog water in the restoration of degraded burned areas under dry Mediterranean conditions, *Agricultural and forest meteorology*, 149, 1896–1906, 2009.
- 530 García, J.-L., Lobos-Roco, F., Schween, J. H., del Río, C., Osses, P., Vives, R., Pezoa, M., Siegmund, A., Latorre, C., Alfaro, F., et al.: Climate and coastal low-cloud dynamic in the hyperarid Atacama fog Desert and the geographic distribution of *Tillandsia landbeckii* (Bromeliaceae) dune ecosystems, *Plant Systematics and Evolution*, 307, 1–22, 2021.
- Garreaud, R., Barichivich, J., Christie, D. A., and Maldonado, A.: Interannual variability of the coastal fog at Fray Jorge relict forests in semiarid Chile, *Journal of Geophysical Research: Biogeosciences*, 113, 2008.
- 535 Garreaud, R., Clem, K., and Veloso, J. V.: The South Pacific pressure trend dipole and the southern blob, *Journal of Climate*, 34, 7661–7676, 2021.
- Goulden, M. L. and Bales, R. C.: California forest die-off linked to multi-year deep soil drying in 2012–2015 drought, *Nature Geoscience*, 12, 632–637, 2019.

- Gultepe, I. and Milbrandt, J.: Microphysical observations and mesoscale model simulation of a warm fog case during FRAM project, in: Fog and boundary layer clouds: Fog visibility and forecasting, pp. 1161–1178, Springer, 2007.
- 540 Gultepe, I., Heymsfield, A. J., Fernando, H., Pardyjak, E., Dorman, C., Wang, Q., Creegan, E., Hoch, S., Flagg, D., Yamaguchi, R., et al.: A review of coastal fog microphysics during C-FOG, *Boundary-Layer Meteorology*, 181, 227–265, 2021.
- Keeley, J. E. and Syphard, A. D.: Large California wildfires: 2020 fires in historical context, *Fire Ecology*, 17, 1–11, 2021.
- Kim, S., Rickard, C., Hernandez-Vazquez, J., and Fernandez, D.: Early Night Fog Prediction Using Liquid Water Content Measurement in  
545 the Monterey Bay Area, *Atmosphere*, 13, 1332, 2022.
- Klemm, O., Schemenauer, R. S., Lummerich, A., Cereceda, P., Marzol, V., Corell, D., Van Heerden, J., Reinhard, D., Gherezghiher, T., Olivier, J., et al.: Fog as a fresh-water resource: overview and perspectives, *Ambio*, 41, 221–234, 2012.
- Koch, M. A., Kleinpeter, D., Auer, E., Siegmund, A., del Rio, C., Osses, P., García, J.-L., Marzol, M. V., Zizka, G., and Kiefer, C.: Living at the dry limits: ecological genetics of *Tillandsia landbeckii* lomas in the Chilean Atacama Desert, *Plant Systematics and Evolution*, 305,  
550 1041–1053, 2019.
- Kogan, F. and Kogan, F.: Monitoring drought from space and food security, *Remote sensing for food security*, pp. 75–113, 2019.
- Koppa, A., Keune, J., and Miralles, D. G.: Are Global Drylands Self-Expanding?, in: EGU General Assembly Conference Abstracts, pp. EGU–2320, 2023.
- Larrain, H., Velásquez, F., Cereceda, P., Espejo, R., Pinto, R., Osses, P., and Schemenauer, R.: Fog measurements at the site “Falda Verde”  
555 north of Chañaral compared with other fog stations of Chile, *Atmospheric Research*, 64, 273–284, 2002.
- Lobos-Roco, F., de Arellano, J. V.-G., and Pedruzo-Bagazgoitia, X.: Characterizing the influence of the marine stratocumulus cloud on the land fog at the Atacama Desert, *Atmospheric research*, 214, 109–120, 2018.
- Lobos-Roco, F., Hartogensis, O., Vilà-Guerau de Arellano, J., De La Fuente, A., Muñoz, R., Rutllant, J., and Suárez, F.: Local evaporation controlled by regional atmospheric circulation in the Altiplano of the Atacama Desert, *Atmospheric Chemistry and Physics Discussions*,  
560 2021, 1–38, 2021.
- Lobos-Roco, F., Suárez, F., Aguirre-Correa, F., Keim, K., Aguirre, I., Vargas, C., Abarca, F., Ramírez, C., Escobar, R., Osses, P., et al.: Understanding inland fog and dew dynamics for assessing potential non-rainfall water use in the Atacama, *Journal of Arid Environments*, 221, 105 125, 2024.
- Lu, M.-L., Conant, W. C., Jonsson, H. H., Varutbangkul, V., Flagan, R. C., and Seinfeld, J. H.: The marine stratus/stratocumulus experiment (MASE): Aerosol-cloud relationships in marine stratocumulus, *Journal of Geophysical Research: Atmospheres*, 112, 2007.
- 565 Malik, F., Clement, R., Gethin, D., Krawszik, W., and Parker, A.: Nature’s moisture harvesters: a comparative review, *Bioinspiration & biomimetics*, 9, 031 002, 2014.
- Masson-Delmotte, V., Zhai, P., Pirani, A., Connors, S. L., Péan, C., Berger, S., Caud, N., Chen, Y., Goldfarb, L., Gomis, M., et al.: Climate change 2021: the physical science basis, Contribution of working group I to the sixth assessment report of the intergovernmental panel on  
570 climate change, 2, 2391, 2021.
- Moat, J., Orellana-Garcia, A., Tovar, C., Arakaki, M., Arana, C., Cano, A., Faundez, L., Gardner, M., Hechenleitner, P., Hepp, J., et al.: Seeing through the clouds—Mapping desert fog oasis ecosystems using 20 years of MODIS imagery over Peru and Chile, *International Journal of Applied Earth Observation and Geoinformation*, 103, 102 468, 2021.
- Montecinos, S., Carvajal, D., Cereceda, P., and Concha, M.: Collection efficiency of fog events, *Atmospheric research*, 209, 163–169, 2018.
- 575 Muñoz, R. C., Zamora, R. A., and Rutllant, J. A.: The coastal boundary layer at the eastern margin of the southeast Pacific (23.4 S, 70.4 W): Cloudiness-conditioned climatology, *Journal of climate*, 24, 1013–1033, 2011.

- Muñoz-Schick, M., Pinto, R., Mesa, A., and Moreira-Muñoz, A.: " Oasis de neblina" en los cerros costeros del sur de Iquique, región de Tarapacá, Chile, durante el evento El Niño 1997-1998, *Revista chilena de historia natural*, 74, 389–405, 2001.
- Painemal, D. and Zuidema, P.: Assessment of MODIS cloud effective radius and optical thickness retrievals over the Southeast Pacific with VOCALS-REx in situ measurements, *Journal of Geophysical Research: Atmospheres*, 116, 2011.
- 580 Roach, W.: Back to basics: Fog: Part 2—The formation and dissipation of land fog, *weather*, 50, 7–11, 1995.
- Schemenauer, R. S. and Cereceda, P.: A proposed standard fog collector for use in high-elevation regions, *Journal of Applied Meteorology and Climatology*, 33, 1313–1322, 1994.
- Schween, J. H., del Rio, C., García, J.-L., Osses, P., Westbrook, S., and Löhnert, U.: Life Cycle of Stratocumulus Clouds over one Year at the Coast of the Atacama Desert, *Atmospheric Chemistry and Physics*, 2022, 1–33, 2022.
- 585 Stull, R. B.: *An introduction to boundary layer meteorology*, vol. 13, Springer Science & Business Media, 2012.
- Verbrugghe, N. and Khan, A. Z.: Water harvesting through fog collectors: a review of conceptual, experimental and operational aspects, *International Journal of Low-Carbon Technologies*, 18, 392–403, 2023.
- Wetzel, P. J.: A simple parcel method for prediction of cumulus onset and area-averaged cloud amount over heterogeneous land surfaces, *Journal of Applied Meteorology and Climatology*, 29, 516–523, 1990.
- 590 Wood, R.: Stratocumulus clouds, *Monthly Weather Review*, 140, 2373–2423, 2012.